PCCP
Physical Chemistry Chemical Physics

Accepted Manuscript

This article can be cited before page numbers have been issued, to do this please use: Y. Liu and H. Vashisth, *Phys. Chem. Chem. Phys.*, 2019, DOI: 10.1039/C9CP04408F.

ROYAL SOCIETY OF CHEMISTRY

rsc.li/pccp

View Article Online
DOI: 10.1039/C9CP04408F

PCCP

ARTICLE TYPE

Cite this: DOI: 00.0000/xxxxxxxxxx

Conformational Dynamics and Interfacial Interactions of Peptide-appended Pillar[5]arene Water Channels in Biomimetic Membranes†

Yong Liu and Harish Vashisth *[a]

Received Date
Accepted Date

DOI: 00.0000/xxxxxxxxxx

Peptide appended pillar[5]arene (PAP) is an artificial water channel resembling biological water channel proteins, which has shown a significant potential for designing bioinspired water purification systems. Given that PAP channels need to be incorporated at a high density in membrane matrices, it is critical to examine the role of channel-channel and channel-membrane interactions in governing the structural and functional characteristics of channels. To resolve the atomic-scale details of these interactions, we have carried out atomistic molecular dynamics (MD) simulations of multiple PAP channels inserted in a lipid or a block-copolymer (BCP) membrane matrix. Classical MD simulations on a sub-microsecond timescale showed clustering of channels only in the lipid membrane, but enhanced sampling MD simulations showed thermodynamically-favorable dimerized states of channels in both lipid and BCP membranes. The dimerized configurations of channels, with an extensive buried surface area, were stabilized via interactions between the aromatic groups in the peptide arms of neighboring channels. The conformational metrics characterizing the orientational and structural changes in channels revealed a higher flexibility in the lipid membrane as opposed to the BCP membrane although hydrogen bonds between the channel and the membrane molecules were not a major contributor to the stability of channels in the BCP membrane. We also found that the channels undergo wetting/dewetting transitions in both lipid and BCP membranes with a marginally higher probability of undergoing a dewetting transition in the BCP membrane. Collectively, these results highlight the role of channel dynamics in governing channel-channel and channel-membrane interfacial interactions, and provide atomic-scale insights needed to design stable and functional biomimetic membranes for efficient separations.

1 Introduction

Protein channels are known to efficiently transport water or ion molecules across cellular membranes with high *in vivo* selectivity. Aquaporins (AQPs) are one family of these protein channels that have also been employed *in vitro* as water channels embedded in synthetic polymeric membranes for designing biomimetic separation materials.[1–5] For example, AqpZ water channel was inserted into a self-assembled synthetic block copolymer (BCP) membrane to achieve high efficiency in water transport.[6] However, laborious and expensive methods of fabrication and low stability of biological water channels make it challenging to integrate them in large-scale applications.[3–5]

Inspired by the separation mechanism of protein channels,[1,5,7–11] self-assembling channels and unimolecular channels are two main types of biomimetic artificial water channels (AWCs) that have been proposed as alternatives to protein channels, primarily due to simplicity of synthesis and low energy input. Among these, self-assembling channels are designed using several building blocks including imidazole quartets,[12,13] dendritic dipeptides,[14,15] hexa(*m*-phenylene ethynylene) molecules,[16] aquafoldamers,[17] and triarylamines[18], while unimolecular channels are typically single supramolecules including carbon nanotubes[19,20] and (peptide or hydrazide) appended pillar[5]arenes.[21–24]

In this work, we have studied molecular details of the functional behavior of a ∼5 Å pore-size peptide-appended pillar[5]arene (PAP) channel (Figure 1A) that can self-assemble into two-dimensional arrays[25,26] and has shown a high water permeability (∼10^8 molecules/s/channel).[21–23,25,26] Specifically, the water permeability values measured for liposomes containing PAP channels were 3.7×10^6 water molecules/s/channel and 3.5×10^8

[a] *Department of Chemical Engineering, University of New Hampshire, 33 Academic Way, Durham, NH 03824, USA. Fax: +1 603-862-3747; Tel: +1 603-862-2483; E-mail: harish.vashisth@unh.edu*

† Electronic Supplementary Information (ESI) available: Additional analyses and snapshots from simulations are provided in Figures S1-S11 in the supporting information. See DOI: 10.1039/cXCP00000x/

View Article Online
DOI: 10.1039/C9CP04408F

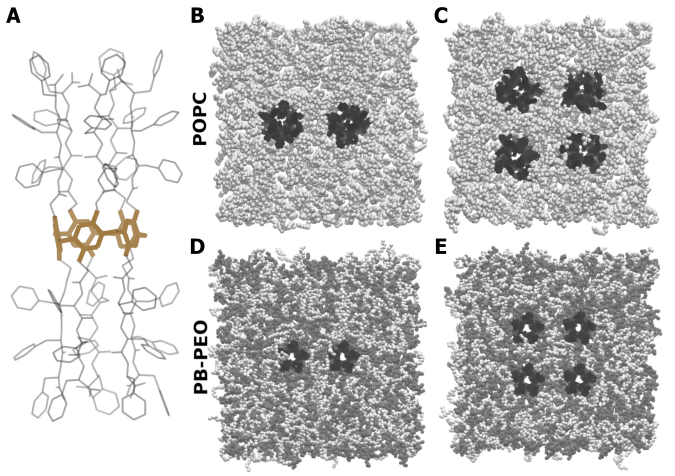

Fig. 1 (A) The molecular structure of the PAP channel is shown with the central pillar-arene ring (brown sticks) and the peptide arms (transparent gray sticks). (B, C, D, and E) Shown are the top-views of four simulation systems in two types of membranes (panels B and C, POPC; and panels D and E, PB-PEO). All molecules are shown in space-filling representations: PAP (black), POPC and PEO chains (white), and PB chains (gray). Water molecules are not shown for clarity.

water molecules/s/channel under vesicle shrinking and swelling conditions, respectively. From a practical membrane design perspective, it is worth noting here that the lipid matrix suffers from low chemical and mechanical stability,[4] but the synthetic counterparts of lipids are amphiphilic BCPs that have been employed as alternative membrane matrices with the ability to assemble water channels into two-dimensional crystals.[5]

In a recent study,[26] we have reported on the conformational dynamics of a single PAP channel in lipid as well as in BCP membranes. We also highlighted that an increase in the length of the hydrophobic block in BCP membranes led to less favorable insertion of the PAP channel likely due to the physical hydrophobic mismatch.[27–29] Moreover, long time-scale molecular dynamics (MD) simulations of a single PAP channel indicated a decrease in the flexibility of the channel in the BCP membrane in comparison to the lipid membrane likely due to the chemical hydrophobic mismatch.[26] However, from an application standpoint, it is desirable to have a higher packing density of channels per unit surface area of the membrane for efficient separations, which significantly increases the likelihood of channel-channel interactions that can alter the conformational and functional behavior of channels. As an example, the proximity of channels due to a denser packing could result in the clustering of channels, where the clusters could be stabilized by a hydrogen bonding network between the phenylalanine chains of neighboring PAPs.[25]

Although the effect of channel-channel interactions and clustering on the permeability and selectivity of the PAP channel remains unknown, keeping channels in their active functional states is a desired characteristic for designing efficient separation systems. Besides the clustering of channels, it is critical to examine perturbations resulting from lipids or polymers which could affect the function of channels.[30] This is evidenced by the observation that the pore of the PAP channel can be blocked by lipid molecules transiently entering the channel pore.[25] Although it is non-trivial to predict the molecular details of the effect of the membrane matrix on channel's functional characteristics, MD simulations are emerging as a useful tool to probe atomistic details of channel-channel and channel-membrane interactions, thereby assisting in the knowledge required to overcome challenges in designing stable membranes.[31]

To address these questions, we report here results from four systems in which multiple PAP channels were inserted in a 1-palmitoyl-2-oleoylphosphatidylcholine (POPC) or a polybutadiene (PB)/polyethylene-oxide (PEO) membrane matrix (Figure 1B-E). To understand channel-channel and channel-membrane interactions in our four systems, we performed long time-scale classical MD simulations totaling 6 μs of simulation time. Besides classical MD simulations, we employed metadynamics as an enhanced sampling method to study the dimerization propensity of two PAP channels and to resolve the thermodynamics of channel dimerization in both lipid and BCP membranes. We also characterized interactions between the channels and their surrounding membrane environment. Our results provide molecular-scale insights into factors that should be considered in designing membranes with a high density of channels while maintaining their activity.

2 Methods

2.1 System Setup

We studied the dynamics of PAP channels in a POPC and a PB-PEO membrane matrix. For each type of membrane, we created two types of systems containing 2 PAP channels (2PAP/POPC and 2PAP/PB-PEO) and 4 PAP channels (4PAP/POPC and 4PAP/PB-PEO) (Figure 1B-E). We used the membrane builder plugin in the Visual Molecular Dynamics (VMD)[32] software to create a square-shaped patch (90 Å $\times$ 90 Å) of the POPC membrane containing 215 lipids before the insertion of PAP channels. After inserting two or four PAP channels with an initial inter-channel center of mass distance of $\sim$30 Å, we removed overlapping lipids within 1.5 Å of each PAP channel. We then obtained 194 and 170 POPC lipids in 2PAP/POPC and 4PAP/POPC systems, respectively. For the BCP membrane, we used the $PB_{12}PEO_9$ architecture which has been successfully used to incorporate PAP channels in our previous work.[26] We placed PB-PEO chains on a grid and arranged them in a diblock configuration over an area of 90 Å $\times$ 90 Å. After inserting two or four PAP channels, similar to systems in the POPC membrane, we obtained 228 and 210 PB-PEO chains in 2PAP/PB-PEO and 4PAP/PB-PEO systems, respectively. We then solvated four systems with explicit water molecules (TIP3P) while keeping the membrane-domains free of water molecules. Details of all systems are given in Table 1.

2.2 Classical MD Simulations

We performed classical MD simulations of our four systems in three stages. In the first stage, after performing an initial minimization of each system for 4000 steps, we performed a brief (0.25 ns; time-step: 1 fs) MD equilibration of lipids and polymers

View Article Online
DOI: 10.1039/C9CP04408F

Table 1 Details of classical MD simulations

#	POPC		PB-PEO	
	2PAP	4PAP	2PAP	4PAP
PAP	2	4	2	4
POPC	194	170	-	-
PB-PEO	-	-	228	210
atoms	55867	53710	84276	83139
water	9467	9330	13692	13783
runs	3	3	3	3
length/run	0.5 μs	0.5 μs	0.5 μs	0.5 μs

in the NVT ensemble. During this first stage, only POPC/PB-PEO atoms were allowed to move while all other atoms were fixed. In the second stage, the initial coordinates of systems from the first step were used to conduct a 0.5 ns MD equilibration of each system with a time-step of 2 fs and in the NPT ensemble at a constant membrane area. All atoms, except those in PAP channels, were allowed to move while additional forces via a tcl-script were applied to keep water molecules out of membranes. In Figure 1 (panels B, C, D, and E), we show snapshots for each system after the second stage. For the final stage, we performed triplicate MD simulations with a time-step of 2 fs in the NPT ensemble for each of our four systems, where each trajectory was 0.5 μs long. We controlled temperature (at 303 K) using a Langevin thermostat and pressure (at 1 atm) using a Nosé-Hoover barostat.

2.3 Metadynamics Simulations

To study the thermodynamics of dimerization of channels in the POPC/PB-PEO membrane matrices, we adopted the initial coordinates of 2PAP/POPC and 2PAP/PB-PEO systems from the last snapshots of the second stage of classical MD simulations. We then employed metadynamics as an enhanced sampling method to resolve the free-energy profiles of two PAP channels dimerizing as a function of the inter-channel distance as a collective variable (CV). Briefly, in metadynamics, a history-dependent biasing potential V_{meta}, defined as a sum of a set of Gaussian functions, is applied[33,34]:

$$V_{\text{meta}}(s) = \sum_{t'=\tau_G,2\tau_G,\ldots}^{t'<t} W \prod_{i=1}^{N_{CV}} \exp\left(-\frac{[s_i - s_i(t')]^2}{2\delta_{s_i}^2}\right) \qquad (1)$$

where, τ_G is the time interval, s_i is the current CV value, $s_i(t')$ is the CV value at $t = t'$, N_{CV} is the number of CVs, W is the height of Gaussian energy packets, and δ is the Gaussian width. In this study, we used one CV (the distance between the central pillar[5]arene rings of two PAP channels: d_{CV}), spanning between 10 Å and 30 Å. We performed metadynamics simulations for both systems with a timestep of 2 fs, W = 0.2 kcal/mol, δ = 0.05 Å, and τ_G = 1 ps, where each trajectory was 0.63 μs long. We have previously applied metadynamics simulations with similar parameters to study several biophysical problems.[35–37] We performed all classical and enhanced sampling MD simulations using NAMD[38], and system setup and analyses using VMD.[32] The force-field parameters for POPC, TIP3P water, and PEO used here are from the CHARMM force-field[39–41], and the parameters for the PAP channel and the PB block were adopted from the literature.[25,42]

2.4 Metrics for Conformational and Functional Analyses

Buried Surface Area (BSA): We used the BSA as a measure to characterize channel-channel interactions. The BSA between a pair of PAP channels, a and b, was measured using the following equation:

$$\text{BSA} = \text{SASA}_\text{a} + \text{SASA}_\text{b} - \text{SASA}_\text{ab} \qquad (2)$$

where SASA_a, SASA_b, and SASA_ab are the solvent accessible surface areas (SASAs) of channel a, channel b, and the pair of channel a and channel b, respectively. A probe radius of 1.4 Å was used to compute SASA. For systems with 2 PAP channels, we measured the BSA between adjacent PAP channels, while for systems with 4 PAP channels, we measured the BSA between adjacent as well as diagonally opposite pairs of PAP channels.

Distance between the Center of Mass (COM) of PAP Channels: We measured two different distances to quantify channel-channel interactions: the distance between the all-atom COM of PAP channels (d_{COM}) and the distance between the central pillar[5]arene rings (d_{CV}). The distance d_{CV} was also used as a CV in metadynamics simulations, where it spans between 10 Å and 30 Å to facilitate observation of dimerization and dissociation of a pair of PAP channels.

Root Mean Squared Distance (RMSD): Since the peptide arms of the PAP channel can undergo structural changes due to perturbations and constraints from each membrane, we evaluated RMSD values of channels in each membrane to quantify conformational changes. The RMSD calculations were based upon all atoms and the initial configuration of the PAP channel was used as a reference.

Orientational Angle: To quantify changes in the orientation of channels, we measured the angle of the channel axis relative to the membrane normal (θ). Initial conformations of channels were perpendicular to the membrane plane ($\theta = 0°$).

Two Dimensional (2D) Number Density: We characterized the dynamics of membranes (POPC or PB-PEO) with 2D number density maps computed over the last 5 ns of each simulation to highlight the distribution of POPC and PB-PEO atoms. By defining grids of 0.5 Å × 0.5 Å size in the xy-plane that span the full z-axis, we counted the number of atoms (N_{atom}) over the last 5 ns and used the following equation to compute the 2D number density:

$$\rho_{\text{atom}} = \text{N}_{\text{atom}}/(\text{N}_{\text{frame}} \times \text{V}) \qquad (3)$$

where ρ_{atom} is the 2D number density in one grid, N_{atom} is the total number of atoms we counted in one grid over the last 5 ns simulation, N_{frame} is the number of frames which is 250, and V is the volume of the chosen slab.

Hydrogen Bonds (H-bonds): We measured the number of

View Article Online
DOI: 10.1039/C9CP04408F

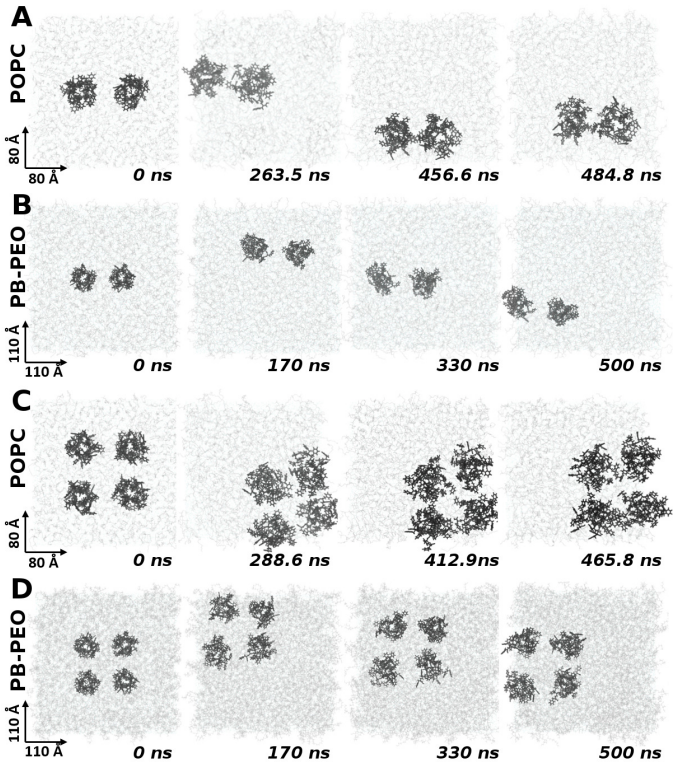

Fig. 2 Snapshots from one of the three MD runs highlighting the evolution of each system at different time points are shown. All panels are labeled, where panels A and B correspond to systems with 2 PAP channels and panels C and D correspond to systems with 4 PAP channels. All PAP channels and membrane molecules are shown in black and gray wireframe representations, respectively.

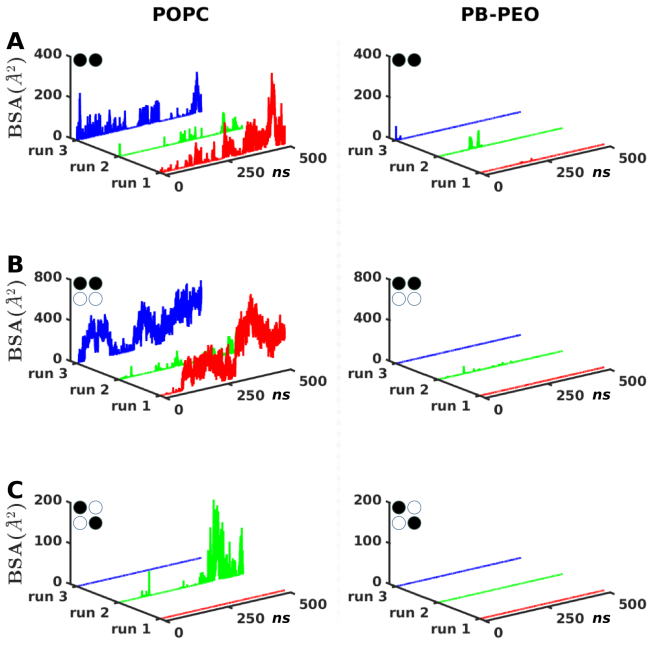

Fig. 3 The evolution of interfacial buried surface area (BSA) *vs.* simulation time (ns) between pairs of PAP channels from three independent runs is shown. Data shown in panels on the left correspond to systems in the POPC membrane, while that on the right correspond to systems in the PB-PEO membrane. The pair of PAP channels for which the BSA is reported are highlighted by filled black circles on the top left corner of each panel. For systems with 4 PAP channels, BSA data are reported for adjacent as well as diagonally opposite channels.

H-bonds (N_H) between the POPC/PB-PEO molecules and each PAP channel using VMD. We used a cutoff distance of 3 Å and a cutoff angle of 20°, and the acceptors of H-bonds included N, S, O, F, C, and P.

Number of Water Molecules: To quantify water transport, wetting, and dewetting characteristics of channels, we computed the number of water molecules (N_W) within PAP channels by defining a cylindrical volume (with diameter = 5 Å and height = 12 Å) centered around the pillar[5]arene ring of each channel.

Permeability: To measure the permeability of each PAP channel in all systems, we applied the collective diffusion model[43] which has been used in previous studies of PAP[25,26] and other proteins.[44] By defining a cylindrical channel volume (3 Å in radius and 8 Å in height) centered around the pillar[5]arene ring of each channel, the mean squared displacement of the collective displacement coordinate $n(t)$ was obtained for each simulation with trajectories divided into 1 ns segments, where $n(0) = 0$ for each segment. The diffusion coefficient of the collective displacement coordinate (D_n) was then used along with the volume of a single water molecule (v_w) to obtain the osmotic permeability of each channel as $v_w D_n$.

3 Results

3.1 Clustering Propensity of Channels

To understand the clustering propensity of channels in membranes, we carried out classical MD simulations of solvated PAP channels in a POPC or a PB-PEO membrane matrix. For each of the four systems, three independent MD simulations (each 0.5 μs long) were carried out, thereby resulting in 6 μs of simulation data. The initial distance between the COM of neighboring PAP channels (d_{COM}) was ~30 Å (Figure 2 at t = 0 ns). In Figure 2, we show snapshots from the conformational evolution of 2PAP and 4PAP systems in POPC (Figures 2A and 2C) and PB-PEO (Figures 2B and 2D) membranes. In the 2PAP/POPC system, we observed clustering of two PAP channels into a dimer after ~263.5 ns simulation (Figure 2A). In fact, a cluster of two PAP channels was observed only after 10 ns in another independent simulation of this system (Figure S1A). We also observed that the cluster size can be up to four PAP channels in the 4PAP/POPC system (Figures 2C and S1B), indicating that a higher density of PAP channels likely increases the propensity of clustering. Compared with the clustering behavior of PAP channels in POPC, the aggregates of PAP channels in PB-PEO (Figures 2B and 2D) were not observed in our classical MD simulations.

Besides the visual inspection of the clustering behavior of channels, we measured the interfacial BSA between a pair of PAP channels (Figures 3, S2A, S2C, and S3) and the distances between

View Article Online
DOI: 10.1039/C9CP04408F

their COM (Figures S2B, S2D, and S4). An increase in the BSA indicates a stronger interaction between a pair of PAP channels. We observed a significant difference between the BSA in the POPC *vs.* PB-PEO membrane. Triplicate runs of the 2PAP/POPC system showed that BSA can be more than 300 Å^2 (Figure 3A; left panel), while the BSA in the 2PAP/PB-PEO system on similar time-scales remains around 0 Å^2 (Figure 3A; right panel).

In the POPC membrane, the BSA of adjacent PAP channels increased with more PAP channels (four channels), as larger values of BSA up to 795 Å^2 were observed (Figure 3B; left panel). Also, a BSA of more than 100 Å^2 between a pair of diagonally opposite PAP channels was identified (Figure 3C; left panel). In contrast to the POPC membrane, the BSAs between pairs of adjacent PAP channels (Figure 3B; right panel) or diagonally placed PAP channels (Figure 3C; right panel) were about 0 Å^2 in 2PAP/4PAP systems in the PB-PEO membrane. The results from other independent simulations in the PB-PEO membrane showed similar behavior (Figures S2 and S3).

These results are further reinforced by measurements on distances between the COM of pairs of PAP channels. Initially, we placed all PAP channels side by side with a d_{COM} of ∼30 Å. The d_{COM} decreased from ∼30 Å to 23 Å when the clustering of PAP channels was observed in the 2PAP/POPC system (Figure S2B), and a shorter d_{COM} of 20 Å was observed in the 4PAP/POPC system (Figure S4). On the contrary, in the PB-PEO membrane we observed that the distances were sufficiently large (30 Å and 40 Å for adjacent and diagonal channels, respectively) to keep PAP channels dissociated (Figures S2D and S4).

3.2 Conformational Flexibility of PAP Channels

We hypothesized that the conformational behavior of PAP channels may alter their functional characteristics. To probe the conformational dynamics of channels in each membrane, we quantified the conformational metrics of the orientational angle (Figure 4) of the channel axis relative to the membrane normal (θ) and the RMSD (Figure 5) relative to the initial structure of the PAP channel (Figure 1A). These variables inform about the conformational flexibility and stabilization of the PAP channel in each membrane.

The initial conformations of PAP channels in all simulations were perpendicular to the membrane plane ($\theta = 0°$). During simulations, the conformations of PAP channels evolved due to interactions with the surrounding lipids or BCPs. In Figure 4, we show distributions of θ for 2PAP and 4PAP systems in both POPC and PB-PEO membranes. These distributions are based upon the data from three independent runs of each system. For the POPC systems (Figure 4A and 4B), we observed that there were two major orientational states for PAP channels corresponding to $\theta = 11°$ and $\theta = 23°$. The predominant orientation of channels in the 2PAP/POPC system was at $\theta = 11°$ (Figure 4A), while in the 4PAP/POPC system was at $\theta = 23°$ (Figure 4B). For the 2PAP/POPC system (Figure 4A), an average θ of ∼18° was observed and θ spanned a range between 0° and 48°. For the 4PAP/POPC system, the averaged θ increased to ∼22°, spanning a range between 0° and 55°. Contrary to relatively wider distributions of θ in the POPC membrane, the distributions in the PB-PEO membrane are sharply peaked (Figure 4C and 4D). The most probable angle was ∼12° for both 2PAP/PB-PEO and 4PAP/PB-PEO systems.

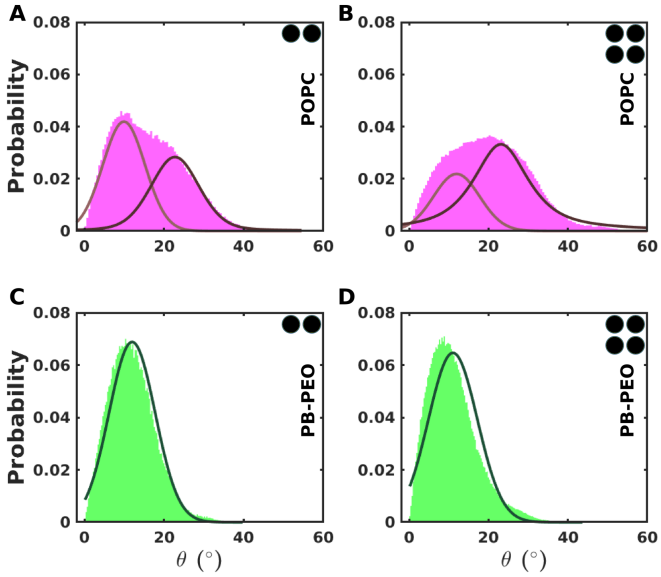

Fig. 4 Probability distributions of the data on the orientational angles (θ) of PAP channels are shown for all four systems (panels A and B, systems in the POPC membrane; and panels C and D, systems in the PB-PEO membrane). The distributions included data on θ values computed from three independent runs. The traces in black indicate the Gaussian functions fitted to describe the data in distributions.

In Figure 5, we show distributions of all-atom RMSD relative to the initial structure (Figure 1A) for all systems in both POPC and PB-PEO membranes. We also show snapshots corresponding to different RMSD values in Figure S5. In the POPC membrane (Figures 5A and 5B), we observed three major states corresponding to RMSD values of ∼5.6 Å, ∼6.1 Å, and ∼6.6 Å, except that in the 4PAP/POPC system, where we also observed a low-populated new state with a higher RMSD value of ∼7.3 Å. The most probable RMSD value was ∼5.6 Å for both 2PAP/POPC and 4PAP/POPC systems.

We also observed that there were three major states, corresponding to RMSDs of ∼4.8 Å, ∼5.2 Å, and ∼6.0 Å, in the 2PAP/PB-PEO system (Figure 5C). However, we observed an additional low-populated state with an RMSD value of 4.5 Å in the 4PAP/PB-PEO system (Figure 5D). The most probable RMSD value for channels in the PB-PEO membrane was 4.8 Å, which is smaller than the RMSD of channels in the POPC membrane (5.6 Å). In addition, the RMSD values up to 8 Å were observed in the POPC membrane, while the largest RMSD was ∼7 Å in the PB-PEO membrane.

3.3 Conformational Behavior of Lipids and BCPs

In all systems, PAP channels were inserted in the hydrophobic regions of membranes and therefore likely affect the arrangements of hydrophobic segments of lipids or BCPs. To probe the arrangement of lipid or BCP molecules surrounding PAP channels, we

View Article Online
DOI: 10.1039/C9CP04408F

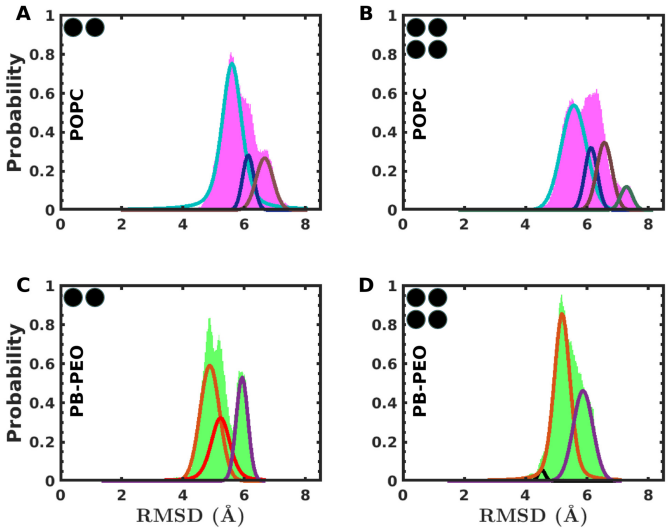

Fig. 5 Data similar to Figure 4 are shown for the distributions of RMSD of PAP channels in all four systems. The distributions included data on RMSD values computed from three independent runs.

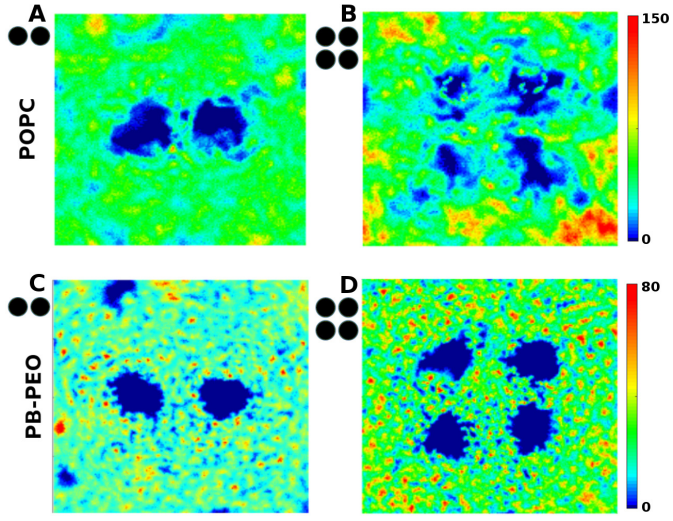

Fig. 6 The 2D number density maps for the hydrophobic tails of lipids or hydrophobic (PB) blocks of BCP membranes are shown. Panels A and B are for systems in the POPC membrane, respectively, and panels C and D are for systems in the PB-PEO membrane. Blue to red color indicates lower to higher values of the number density (ranging between 0 and 150 $Å^{-3}$ for the POPC membrane and between 0 and 80 $Å^{-3}$ for the PB-PEO membrane).

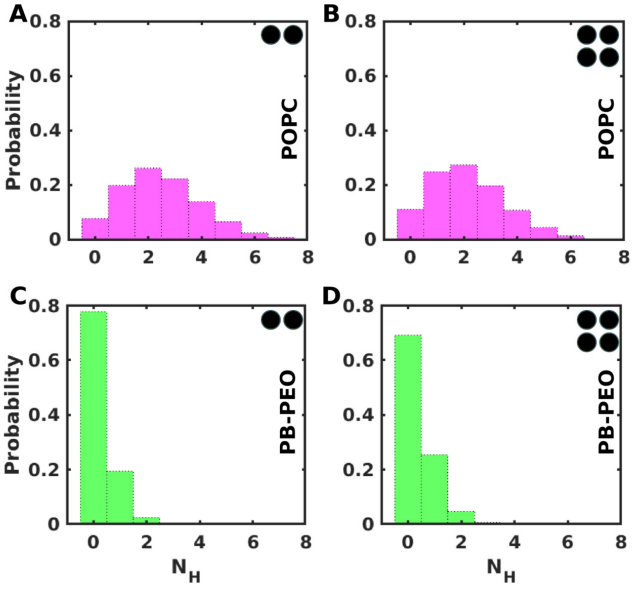

Fig. 7 Probability distributions of the data on the number of hydrogen bonds (N_H) between the PAP channel and the surrounding POPC or PB-PEO matrix are shown for all four systems (panels A and B, systems in the POPC membrane; and panels C and D, systems in the PB-PEO membrane). The distributions included data on N_H averaged over all PAP channels and three independent runs.

first analyzed (over the last 5 ns in all simulations) the 2D atomic number density for the hydrophobic regions of POPC or PB-PEO molecules. In Figure 6, we show color-coded atomic density maps for 2PAP and 4PAP systems, where blue indicates lower densities and red indicates higher densities. For systems in the POPC membrane (Figures 6A and 6B), we observed larger areas with uniform colors (similar densities) indicating that lipid molecules likely diffuse in a larger volume instead of localizing in a specific region. However, in the PB-PEO membrane (Figures 6C and 6D), we observed that the atomic density maps have many small patches of isolated areas with yellow-to-red color indicating a higher local density of atoms. These observations are further corroborated by measurements on radially distributed positions of the center of mass of lipid and BCP molecules surrounding PAP channels which showed that some of the lipid molecules that were initially closer to the PAP channel diffused significantly away (Figure S7A) during the course of simulation, while the PB-PEO chains mostly stayed near the channel (Figure S7B).

3.4 Hydrogen-bonding Interactions

To understand the interactions of PAP channels with the lipid or BCP molecules, we analyzed hydrogen-bonding interactions because non-covalent H-bonds are assumed as a major contributor to structural stabilization in biological systems.[45,46] Therefore, it has been suggested that water channels could be stabilized through the formation of H-bonds between the channel and membrane molecules.[30] Specifically, we investigated the number of hydrogen-bonds (N_H) between the PAP channel and POPC or PB-PEO molecules (Figure 7). We observed N_H values up to 8 for systems in the POPC membrane, although the mean value of N_H

View Article Online
DOI: 10.1039/C9CP04408F

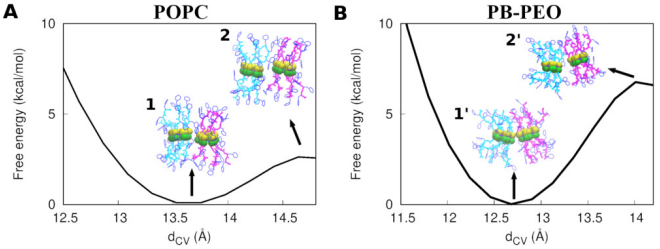

Fig. 8 Free-energy profiles of channel dimerization in each membrane (panel A, POPC; and panel B, PB-PEO) are plotted against the chosen collective variable (d_{CV}). The free-energy scale is plotted to have the free-energy minimum in each profile corresponding to a free energy value of zero. Shown also are side-view snapshots of both PAP channels at the free-energy minima (labeled 1 and 1′) and at the free-energy barrier (labeled 2 and 2′) to dissociation. The central pillar[5]arene rings are colored as yellow or green spheres, the backbone of the peptide arms of each channel is colored as cyan or magenta sticks, and the aromatic rings in each peptide arm are colored in blue sticks. The corresponding top-views of channel snapshots are shown in Figure S7.

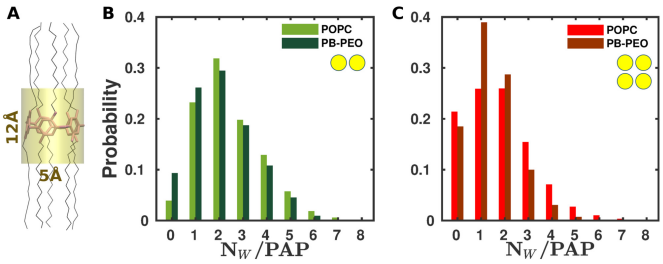

Fig. 9 (A) The channel volume selected for measuring the number of water molecules (N_w) is highlighted as a transparent cylinder centered around the pillar-arene ring of the PAP channel. (B and C) Probability distributions of N_w are shown for 2PAP configurations (panel B) and 4PAP configurations (panel C) in each membrane. The distributions were computed from data averaged over all PAP channels and from three independent MD simulations.

was 2 (Figure 7A, B). However, increased number of PAP channels did not result in an increase in N_H, which is likely because channel-channel interactions led to a decreased contact area between the channels and lipids. On the contrary, for systems in the BCP membrane, we observed the highest probability for the occurrence of no hydrogen bonds and significantly lower probabilities for 1 or 2 hydrogen bonds. Unlike systems in the POPC membrane, this suggests that the hydrogen bonds between the PAP channel and the PB-PEO molecules are likely not a major contributor to the flexibility and/or stability of the channel in the BCP membrane.

3.5 Thermodynamic Analysis of PAP Dimerization

While we observed the spontaneous dimerization of PAP channels in the POPC membrane in our classical MD simulations (Figure 2), we did not observe it in the PB-PEO membrane on a 0.5 μs timescale. Therefore, we used metadynamics as an enhanced sampling method for studying the dimerization propensity of a pair of PAP channels in each type of membrane, where two channels were initially placed at a distance of 30 Å. In Figure 8, we show free-energy profiles as a function of the chosen CV (d_{CV}; see methods) as well as the snapshots of both channels at the minima (near association) and the maxima (near dissociation).

Each profile shows a free energy minimum where stable PAP-dimers were formed in the POPC membrane (Figure 8A; d_{CV} ~13.6 Å) and in the PB-PEO membrane (Figure 8B; d_{CV} ~12.7 Å). The dimerized configuration of channels at each free energy minimum suggests that two PAP channels were adjacently positioned (Figure 8 and Figure S7), while a further decrease in d_{CV} to lower values shows an increase in the free energy (Figure 8) and thereby distortions in channels (Figure S8). For the dimerized configurations, the BSA between the channels was 1032 Å^2 (POPC) and 918 Å^2 (PB-PEO) which indicates an extensive dimerization interface.

From each free energy profile, one can further infer the free energy barrier that needs to be overcome for the dissociation of dimerized configurations. This barrier is the free energy difference between the energy maxima observed at higher values of d_{CV} (occurring at ~14.6 Å in POPC, and at ~14 Å in PB-PEO) and the minima corresponding to the dimerized states. These barriers are ~3 kcal/mol (in the POPC membrane) and ~7 kcal/mol (in the PB-PEO membrane) indicating that the dimerized channels are less likely to dissociate in the PB-PEO membrane relative to that in the POPC membrane.

3.6 Water Transport Characteristics

It is of interest to understand the influence of membranes on the functional transport behavior of PAP channels. To quantify this, we measured the averaged number of water molecules in all PAP channels over three independent classical MD simulations. Specifically, we counted the number of water molecules within a cylindrical volume (Figure 9A) centered around the pillar[5]arene ring of each channel. When two PAP channels were inserted in each membrane, the most probable scenario was the presence of two water molecules (Figure 9B). The probability of observing states with no water molecules within the cylindrical volume was marginally higher in the 2PAP/PB-PEO system than in the 2PAP/POPC system.

We also observed that the increased density of PAP channels affected their water transport characteristics. The systems with a higher density of PAP channels showed a marginally higher probability of observing the state with no water residence (Figure 9C): the probability of a drying state increased from 4% to 22% for systems in the POPC membrane, and from 10% to 18% for systems in the PB-PEO membrane. More than four fold increase (from 4% to 22%) in the probability of no water residence in the POPC membrane indicates that stronger channel-channel interactions in the 4PAP/POPC system in comparison to the 2PAP/POPC system may pose a blocking effect on water transport.

Furthermore, we measured the osmotic water permeability of individual PAP channels in each system for each simulation (Figure 10). We observed an averaged permeability of 2.99×10^{-14} cm^3/s/channel in the 2PAP/POPC system (Figure 10A), while the averaged permeability slightly decreased to 2.89×10^{-14} cm^3/s/channel in the 4PAP/POPC system (Fig-

View Article Online
DOI: 10.1039/C9CP04408F

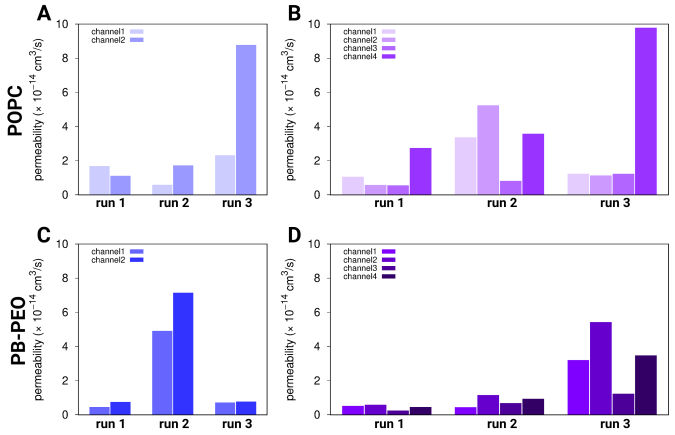

Fig. 10 Permeability of each PAP channel in both POPC (panel A, 2PAP/POPC; and panel B, 4PAP/POPC) and PB-PEO (panel C, 2PAP/PB-PEO; and panel D, 4PAP/PB-PEO) membranes. The permeability values for each channel are reported from three independent simulations.

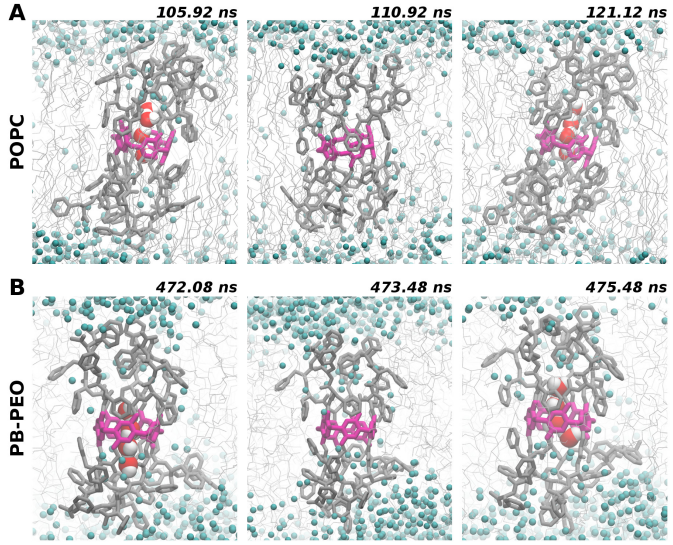

Fig. 11 Snapshots of wetting/dewetting states of a single PAP channel are shown in the POPC membrane (panel A; wetting states: 105.92 ns and 121.12 ns, and the dewetting state: 110.92 ns) and in the PB-PEO membrane (panel B; wetting states: 472.08 and 475.48 ns, and the dewetting state: 473.48 ns). In all snapshots, depicted are PAP channels via gray/magenta sticks, lipids/BCP molecules via gray lines, neighboring water molecules via cyan spheres, and water molecules inside channels in van der Waals representations (oxygen atoms in red and hydrogen atoms in white).

ure 10B). The averaged permeability for the 2PAP/PB-PEO system was 2.72×10^{-14} cm^3/s/channel (Figure 10C) and decreased to 1.70×10^{-14} cm^3/s/channel the 4PAP/PB-PEO system (Figure 10D). While these permeability values are of the same order of magnitude as observed in our previous study of a single PAP channel in both membranes,[26] individual PAP channels showed significant differences in permeability values: the lowest and the highest permeability values respectively were 0.58 $\times 10^{-14}$ cm^3/s and 8.77 $\times 10^{-14}$ cm^3/s (2PAP/POPC), 0.55 $\times 10^{-14}$ cm^3/s and 9.78 $\times 10^{-14}$ cm^3/s (4PAP/POPC), 0.45 $\times 10^{-14}$ cm^3/s and 7.14 $\times 10^{-14}$ cm^3/s (2PAP/PB-PEO), and 0.24 $\times 10^{-14}$ cm^3/s and 5.42 $\times 10^{-14}$ cm^3/s (4PAP/PB-PEO). Correspondingly, we also observed in each membrane that the PAP channel with a higher permeability has a lower mean RMSD, while the one with a lower permeability has a higher mean RMSD (Figure S9), thereby suggesting a correlation between the channel flexibility and its permeability.

Furthermore, we observed wetting/dewetting transitions in PAP channels in both membranes, where fully transitioning from a dewetting state to a wetting state required less than 3 ns (Figure 11). Such transitions have been explained as capillary condensation switching with capillary evaporation, as observed in AQPs and AWCs.[47,48] These observations highlight that water molecules in PAP channels are likely in a metastable state. The transport characteristics of the PAP channel can be further affected by the membrane molecules. Unlike a previous study in which it was observed that a lipid chain could enter the PAP channel and block its pore,[25] in our simulations we did not observe that the entrances/exits of PAP channels were completely blocked by lipid molecules or the PB-PEO chains, although we observed that the entrance of each PAP channel was partially or transiently blocked by the flexible arms of the channel itself or the hydrophilic regions of lipids or polymer chains.

3.7 Conformational Metrics and Water Transport Characteristics in Larger Systems

To test the effect of the membrane-size on conformational metrics and water transport characteristics of PAP channels, we further studied two larger systems, 2PAP/POPC (85423 atoms) and 4PAP/POPC (83766 atoms), with increased number of POPC lipids (383 and 363 lipids, respectively). We conducted two independent simulations for each system with each simulation trajectory of 300 ns (2PAP/POPC) and 100 ns (4PAP/POPC), respectively. In both systems, we observed clustering of PAP channels (Figures S10A, S11A) with the interfacial BSA up to 400 Å^2 (Figures S10B, S11B). With an increased density of PAP channels, we observed that the distributions of conformational metrics (θ and RMSD) became more wider (panels C, D in Figure S10 *vs.* Figure S11) and the range of values explored for both metrics were consistent with the data from systems with lower number of lipids (panels A, B in Figures 4, 5). We further measured water permeability of each PAP channel in both systems and report an averaged permeability of 1.61×10^{-14}cm^3/s with a range between 1.03×10^{-14}cm^3/s and 2.05×10^{-14}cm^3/s in the 2PAP/POPC system, and an averaged permeability of 1.50×10^{-14}cm^3/s with a range between 0.71×10^{-14}cm^3/s and 2.54×10^{-14}cm^3/s in the 4PAP/POPC system.

4 Discussion

In this study, we incorporated multiple PAP channels in a lipid or a polymeric membrane and employed classical MD simulations and enhanced sampling methods to investigate channel-channel and channel-membrane interactions. The results show clustering

View Article Online
DOI: 10.1039/C9CP04408F

of PAP channels in the POPC membrane in classical MD simulations. The clustering phenomenon was highlighted in a recent study, in which it was suggested that the aggregates were stabilized by hydrogen bonds between neighboring PAP channels.[25] We observed that the interaction between PAP channels initially occurred through the aromatic rings of the peptide arms in channels. Therefore, we note that the π-π stacking of aromatic rings from neighboring channels also contributes to the stabilization of aggregates.

Moreover, an increased density of channels could result in stronger interfacial interactions between PAP channels, thereby subsequently leading to a large-size cluster, as seen in this study where a cluster of four PAP channels was formed, and in a recent work[25] where the size of a PAP cluster in lipids could be up to 13 PAP channels. The interfacial BSA between the channels in the 2PAP/POPC system was up to 300 Å^2 *vs.* 795 Å^2 in the 4PAP/POPC system which suggests that a higher density of PAP channels leads to interfacial channel-channel interactions over a larger area.

We also note that the timescale of 0.5 μs was not sufficient for observing via classical MD simulations the clustering of channels in the PB-PEO membrane, as the observation of clustering of PAP channels likely requires overcoming higher free energy barriers. However, the free energy profiles resolved via enhanced sampling metadynamics simulations showed that the dimerized states of PAP channels exist in both POPC and PB-PEO membranes. While the dissociation of a PAP dimer requires overcoming a barrier of $\sim$3 kcal/mol in the POPC membrane, up to $\sim$7 kcal/mol is required for the dimer dissociation in the PB-PEO membrane.

We observed that the increased density of PAP channels could also affect the orientation of channels in the POPC membrane while a little effect was observed in the BCP membrane. Our previous study of a single PAP channel in the POPC/PB-PEO membrane suggested that the tile-angle (θ) of the axis of the PAP channel, relative to the membrane normal, was $\sim$15°.[26] In this study, the averaged tilt-angles were found higher when two or four PAP channels were inserted in the POPC membrane: 18° in the 2PAP/POPC system and 22° in the 4PAP/POPC system. We also observed that the tilt-angle distributions of channels in the POPC membrane became broader when the number of channels was increased from two to four. However, in the PB-PEO membrane, the averaged tilt-angle for channels was $\sim$12° and no significant changes in tilt-angles were observed when the channel density was increased from two to four.

Furthermore, based upon all-atom RMSD calculations, we found that the channels were more flexible in the POPC membrane than in the PB-PEO membrane and increasing the channel density in the POPC membrane led to higher RMSD values. Our previous study of a single PAP channel demonstrated that the RMSD values in PAP channels are mostly contributed by the flexible peptide arms,[26] which suggests that the peptide arms in channels were more stable in the PB-PEO membrane relative to the POPC membrane. This is potentially useful for the design of PAP-based biomimetic membranes where it is desired to enhance the stability of channels while maintaining their functional (permeability/selectivity) characteristics.

Unlike the studies on carbon nanotubes (CNTs) in lipids where the surrounding lipid molecules adopted a layered and annular structure,[49] we did not observe any organized pattern from the analysis of two-dimensional atomic densities of POPC or PB-PEO molecules. This observation is consistent with the viewpoint that the flexibility and roughness of the outer wall of a biological/synthetic channel plays a vital role in lipid distributions and the increased flexibility of the outer wall may deteriorate the organization of membrane molecules.[30,50–54] The arms of the PAP channel are flexible without a well-defined shape unlike the rigid structure of a CNT, indicating that the perturbations on membranes due to the PAP channel are likely smaller than those by a CNT.[30] Moreover, multiple clustered channels as a single assembly may further increase the surface roughness, thereby affecting the organization of lipid or BCP molecules.

We also identified that the probability of observing a dewetting state in the PAP channel is marginally higher than in the PB-PEO membrane compared to the POPC membrane. This is consistent with our previous study showing that the permeability of PAP channels in the PB-PEO membrane was slightly lower than in the POPC membrane, although the value of the channel permeability in each membrane was of the same order of magnitude ($\sim 10^8$ molecules/s/channel).[26] Furthermore, we observed a higher probability of observing a dewetting state when the channel density was higher. Specifically, an increase of up to $\sim$20% in the probability of observing a dewetting state was found in both 4PAP/POPC and 4PAP/PB-PEO systems. A previous study also suggested that from a set of 25 PAP channels inserted in the POPC membrane, on average, only 40% of the channels were filled with water.[25] Our single-channel osmotic permeability measurements for individual PAP channels (Figure 10) further revealed differences in their water permeability characteristics, which correlated well with the flexibility of the channel in that the channels with higher/lower permeability values had lower/higher RMSD values (Figure S9), respectively.

These observations mean that the PAP channel, like other hydrophobic nanopores, likely functions via a gating mechanism and switches between an open and a closed state.[19,55] This nanopore confinement effect leads to perturbed diffusive and dielectric behavior of water molecules,[47,56,57] and thereby leads to a wetting/dewetting transition in the channel. We aim to report on detailed studies of these transitions in our future work. While water orientation and interactions with the channel interior are factors leading to a dewetting state, other factors could be the blockage of the channel pore by membrane molecules.[25] Collectively, these results reveal several atomic-scale details of channel-channel and channel-membrane interactions[58,59] that govern the functional behavior of channels and are therefore key factors to consider in the design of biomimetic membranes with a high density of channels.

5 Conclusions

We employed MD simulations to study channel-channel and channel-membrane interactions of AWCs in lipid and BCP membranes. Specifically, we incorporated multiple PAP channels in a POPC or a PB-PEO membrane matrix to investigate interfacial in-

View Article Online
DOI: 10.1039/C9CP04408F

teractions between channels and membranes. Although classical MD simulations on a 0.5 μs timescale showed spontaneous clustering of channels only in the POPC membrane, enhanced sampling simulations showed that it is thermodynamically favorable for channels to dimerize in both POPC and PB-PEO membranes. We found that the free-energy barrier for the dissociation of dimerized channels was ∼4 kcal/mol higher in the PB-PEO membrane relative to the POPC membrane. We quantified that the dimerized configurations have ∼1000 Å^2 of surface area buried between the channels and the neighboring channels are stabilized by π-π interactions between the aromatic groups in the peptide arms of each channel. The measurements on the tilt-angle of the channel axis and the RMSD relative to the initial structure showed that the channels were more flexible in the POPC membrane relative to the PB-PEO membrane. We also found that the hydrogen bonds between the channel and the membrane molecules were not a major contributor to channel stability in the PB-PEO membrane. Furthermore, we report on wetting/dewetting transitions in the PAP channel in both POPC and PB-PEO membranes and found that the probability of observing a dewetting state was marginally higher at a higher channel density and for channels in the PB-PEO membrane.

Conflicts of interest

There are no conflicts to declare.

Acknowledgements

We acknowledge computational support through the following resources: Premise, a central shared HPC cluster at UNH supported by the Research Computing Center; BioMade, a heterogeneous CPU/GPU cluster supported by the NSF EPSCoR award (OIA-1757371); and the NSF-supported (ACI-1548562) Extreme Science and Engineering Discovery Environment (XSEDE)[60] Comet resource at San Diego Supercomputer Center (SDSC) under grant TG-MCB160183 (HV).

Notes and references

1 P. Agre, *Angew. Chem. Int. Ed.*, 2004, **43**, 4278–4290.
2 J. Eliasson, *Nature*, 2015, **517**, 6–7.
3 I. Kocsis, Z. Sun, Y. M. Legrand and M. Barboiu, *npj Clean Water*, 2018, **1**, 13.
4 Y.-x. Shen, P. O. Saboe, I. T. Sines, M. Erbakan and M. Kumar, *J. Membrane Sci.*, 2014, **454**, 359–381.
5 W. Song, C. Lang, Y.-x. Shen and M. Kumar, *Annu. Rev. Mater. Res.*, 2018, **48**, 57–82.
6 M. Kumar, M. Grzelakowski, J. Zilles, M. Clark and W. Meier, *Proc. Natl. Acad. Sci. U. S. A.*, 2007, **104**, 20719–20724.
7 B. Hille, *Ion channels of excitable membranes*, Sinauer Sunderland, MA, 2001, vol. 507.
8 K. Murata, K. Mitsuoka, T. Hirai, T. Walz, P. Agre, J. B. Heymann, A. Engel and Y. Fujiyoshi, *Nature*, 2000, **407**, 599–605.
9 H. Chen, B. Ilan, Y. Wu, F. Zhu, K. Schulten and G. A. Voth, *Biophys. J.*, 2007, **92**, 46–60.
10 K. Gopinadhan, S. Hu, A. Esfandiar, M. Lozada-Hidalgo, F. C. Wang, Q. Yang, A. V. Tyurnina, A. Keerthi, B. Radha and A. K. Geim, *Science*, 2019, **363**, 145–148.
11 H. B. Park, J. Kamcev, L. M. Robeson, M. Elimelech and B. D. Freeman, *Science*, 2017, **356**, eaab0530.
12 Y. Le Duc, M. Michau, A. Gilles, V. Gence, Y.-M. Legrand, A. van der Lee, S. Tingry and M. Barboiu, *Angew. Chem. Int. Ed.*, 2011, **50**, 11366–11372.
13 E. Licsandru, I. Kocsis, Y.-x. Shen, S. Murail, Y.-M. Legrand, A. Van Der Lee, D. Tsai, M. Baaden, M. Kumar and M. Barboiu, *J. Am. Chem. Soc.*, 2016, **138**, 5403–5409.
14 V. Percec, A. E. Dulcey, V. S. Balagurusamy, Y. Miura, J. Smidrkal, M. Peterca, S. Nummelin, U. Edlund, S. D. Hudson, P. A. Heiney, D. Hu, S. N. Magonov and S. A. Vinogradov, *Nature*, 2004, **430**, 764–768.
15 M. S. Kaucher, M. Peterca, A. E. Dulcey, A. J. Kim, S. A. Vinogradov, D. A. Hammer, P. A. Heiney and V. Percec, *J. Am. Chem. Soc.*, 2007, **129**, 11698–11699.
16 X. Zhou, G. Liu, K. Yamato, Y. Shen, R. Cheng, X. Wei, W. Bai, Y. Gao, H. Li, Y. Liu, F. Liu, D. M. Czajkowsky, J. Wang, M. J. Dabney, Z. Cai, J. Hu, F. V. Bright, L. He, X. C. Zeng, Z. Shao and B. Gong, *Nat. Commun.*, 2012, **3**, 949.
17 H. Zhao, S. Sheng, Y. Hong and H. Zeng, *J. Am. Chem. Soc.*, 2014, **136**, 14270–14276.
18 S. Schneider, E.-D. Licsandru, I. Kocsis, A. Gilles, F. Dumitru, E. Moulin, J. Tan, J.-M. Lehn, N. Giuseppone and M. Barboiu, *J. Am. Chem. Soc.*, 2017, **139**, 3721–3727.
19 G. Hummer, J. C. Rasaiah and J. P. Noworyta, *Nature*, 2001, **414**, 188–190.
20 R. H. Tunuguntla, R. Y. Henley, Y.-C. Yao, T. A. Pham, M. Wanunu and A. Noy, *Science*, 2017, **357**, 792–796.
21 W. Si, L. Chen, X.-B. Hu, G. Tang, Z. Chen, J.-L. Hou and Z.-T. Li, *Angew. Chem. Int. Ed.*, 2011, **123**, 12772–12776.
22 X.-B. Hu, Z. Chen, G. Tang, J.-L. Hou and Z.-T. Li, *J. Am. Chem. Soc.*, 2012, **134**, 8384–8387.
23 L. Chen, W. Si, L. Zhang, G. Tang, Z.-T. Li and J.-L. Hou, *J. Am. Chem. Soc.*, 2013, **135**, 2152–2155.
24 N. Song, T. Kakuta, T.-a. Yamagishi, Y.-W. Yang and T. Ogoshi, *Chem*, 2018, **4**, 2029–2053.
25 Y.-x. Shen, W. Si, M. Erbakan, K. Decker, R. De Zorzi, P. O. Saboe, Y. J. Kang, S. Majd, P. J. Butler, T. Walz, A. Aksimentiev, J.-l. Hou and M. Kumar, *Proc. Natl. Acad. Sci. U. S. A.*, 2015, **112**, 9810–9815.
26 Y.-x. Shen, W. C. Song, D. R. Barden, T. Ren, C. Lang, H. Feroz, C. B. Henderson, P. O. Saboe, D. Tsai, H. Yan, P. J. Butler, G. C. Bazan, W. A. Phillip, R. J. Hickey, P. S. Cremer, H. Vashisth and M. Kumar, *Nat. Commun.*, 2018, **9**, 2294.
27 O. Mouritsen and M. Bloom, *Biophys. J.*, 1984, **46**, 141–153.
28 M. Sperotto and O. Mouritsen, *Eur. Biophys. J*, 1988, **16**, 1–10.
29 M. Ø. Jensen and O. G. Mouritsen, *Biochim. Biophys. Acta, Biomembr.*, 2004, **1666**, 205–226.
30 R. Garcia-Fandiño, A. Piñeiro, J. L. Trick and M. S. Sansom, *ACS Nano*, 2016, **10**, 3693–3701.
31 A. Makarucha, N. Todorova and I. Yarovsky, *Eur. Biophys. J.*, 2011, **40**, 103–115.

View Article Online
DOI: 10.1039/C9CP04408F

32 W. Humphrey, A. Dalke and K. Schulten, *J. Mol. Graphics*, 1996, **14**, 33–38.

33 A. Laio and M. Parrinello, *Proc. Natl. Acad. Sci. U. S. A.*, 2002, **99**, 12562–12566.

34 A. Laio and F. L. Gervasio, *Rep. Prog. Phys.*, 2008, **71**, 126601.

35 H. Mohammadiarani and H. Vashisth, *Front. Endocrinol.*, 2016, **7**, 68.

36 H. Mohammadiarani and H. Vashisth, *J. Comput. Chem.*, 2017, **38**, 1158–1166.

37 M. Mohammadi, H. Mohammadiarani, V. S. Shaw, R. R. Neubig and H. Vashisth, *Proteins*, 2019, **87**, 146–156.

38 J. C. Phillips, R. Braun, W. Wang, J. Gumbart, E. Tajkhorshid, E. Villa, C. Chipot, R. D. Skeel, L. Kale and K. Schulten, *J. Comput. Chem.*, 2005, **26**, 1781–1802.

39 A. D. MacKerell Jr, D. Bashford, M. Bellott, R. L. Dunbrack Jr, J. D. Evanseck, M. J. Field, S. Fischer, J. Gao, H. Guo, S. Ha, D. Joseph-McCarthy, L. Kuchnir, K. Kuczera, F. T. K. Lau, C. Mattos, S. Michnick, T. Ngo, D. T. Nguyen, B. Prodhom, W. E. Reiher, B. Roux, M. Schlenkrich, J. Smith, R. Stote, J. Straub, M. Watanabe, J. Wirkiewicz-Kuczera, D. Yin and M. Karplus, *J. Phys. Chem. B*, 1998, **102**, 3586–3616.

40 K. Vanommeslaeghe, E. Hatcher, C. Acharya, S. Kundu, S. Zhong, J. Shim, E. Darian, O. Guvench, P. Lopes, I. Vorobyov *et al.*, *J. Comp. Chem.*, 2010, **31**, 671–690.

41 J. Huang, S. Rauscher, G. Nawrocki, T. Ran, M. Feig, B. L. de Groot, H. Grubmüller and A. D. MacKerell Jr, *Nature Methods*, 2017, **14**, 71.

42 D. R. Barden and H. Vashisth, *Faraday Discuss.*, 2018, **209**, 161–178.

43 F. Zhu, E. Tajkhorshid and K. Schulten, *Phys. Rev. Lett.*, 2004, **93**, 224501.

44 M. Ø. Jensen and O. G. Mouritsen, *Biophys. J.*, 2006, **90**, 2270–2284.

45 C. L. Perrin and J. B. Nielson, *Annu. Rev. Phys. Chem.*, 1997, **48**, 511–544.

46 Y. Liu, L. Chen, T. Wang, Q. Zhang, C. Wang, J. Yan and L. Ma, *ACS Sustainable Chem. Eng.*, 2015, **3**, 1745–1755.

47 O. Beckstein and M. S. Sansom, *Proc. Natl. Acad. Sci. U. S. A.*, 2003, **100**, 7063–7068.

48 M. Sotomayor and K. Schulten, *Biophys. J.*, 2004, **87**, 3050–3065.

49 M. Vögele, J. Köfinger and G. Hummer, *Faraday Discuss.*, 2018, **209**, 341–358.

50 P. S. NiemelaÌĹ, M. S. Miettinen, L. Monticelli, H. Hammaren, P. Bjelkmar, T. Murtola, E. Lindahl and I. Vattulainen, *J. Am. Chem. Soc.*, 2010, **132**, 7574–7575.

51 E. Lindahl and O. Edholm, *Phys. Rev. E*, 1998, **57**, 791–796.

52 M. Lelimousin and M. S. Sansom, *Small*, 2013, **9**, 3639–3646.

53 R. García-Fandiño and M. S. Sansom, *Proc. Natl. Acad. Sci. U. S. A.*, 2012, **109**, 6939–6944.

54 J. Liu and A. J. Hopfinger, *Chem. Res. Toxicol.*, 2008, **21**, 459–466.

55 J. C. Rasaiah, S. Garde and G. Hummer, *Annu. Rev. Phys. Chem.*, 2008, **59**, 713–740.

56 S. Rao, C. I. Lynch, G. Klesse, G. E. Oakley, P. J. Stansfeld, S. J. Tucker and M. S. Sansom, *Faraday Discuss.*, 2018, **209**, 231–247.

57 O. Beckstein, P. C. Biggin and M. S. Sansom, *J. Phys. Chem. B*, 2001, **105**, 12902–12905.

58 A. Lee, *Biochim. Biophys. Acta Biomembr.*, 2003, **1612**, 1–40.

59 A. W. Smith, *Biochim. Biophys. Acta Biomembr.*, 2012, **1818**, 172–177.

60 J. Towns, T. Cockerill, M. Dahan, I. Foster, K. Gaither, A. Grimshaw, V. Hazlewood, S. Lathrop, D. Lifka, G. D. Peterson, R. Roskies, J. R. Scott and N. Wilkins-Diehr, *Comput. Sci. Eng.*, 2014, **16**, 62–74.

View Article Online
DOI: 10.1039/C9CP04408F

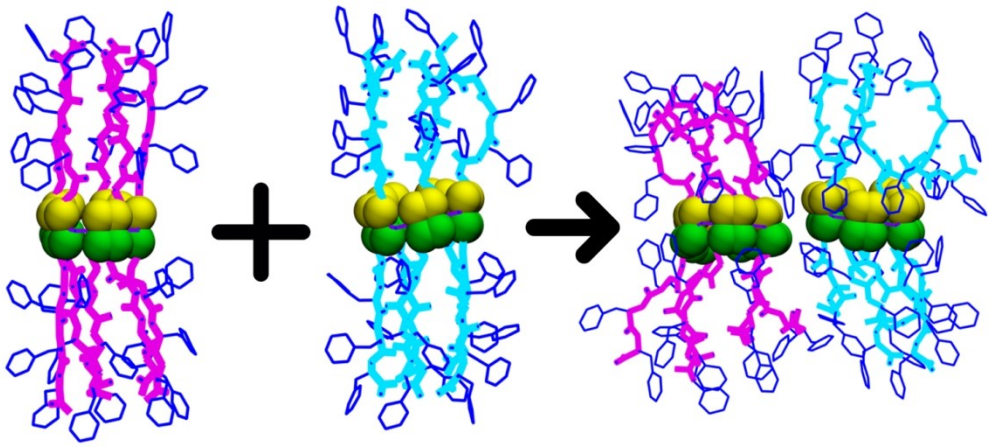

534x238mm (72 x 72 DPI)